

## NUMERICAL STUDIES OF IMPURITIES IN FUSION PLASMAS\*

R. A. Hulse

Plasma Physics Laboratory, Princeton University

Princeton, New Jersey 08544

## ABSTRACT

The coupled partial differential equations used to describe the behavior of impurity ions in magnetically confined controlled fusion plasmas require numerical solution for cases of practical interest. Computer codes developed for impurity modeling at the Princeton Plasma Physics Laboratory are used as examples of the types of codes employed for this purpose. These codes solve for the impurity ionization state densities and associated radiation rates using atomic physics appropriate for these low-density, high-temperature plasmas. The simpler codes solve local equations in zero spatial dimensions while more complex cases require codes which explicitly include transport of the impurity ions simultaneously with the atomic processes of ionization and recombination. Typical applications are discussed and computational results are presented for selected cases of interest.

## DISCLAIMER

This report was prepared as an account of work sponsored by an agency of the United States Government. Neither the United States Government nor any agency thereof, nor any of their employees, makes any warranty, express or implied, or assumes any legal liability or responsibility for the accuracy, completeness, or usefulness of any information, apparatus, product, or process disclosed, or represents that its use would not infringe privately owned rights. Reference herein to any specific commercial product, process, or service by trade name, trademark, manufacturer, or otherwise, does not necessarily constitute or imply its endorsement, recommendation, or favoring by the United States Government or any agency thereof. The views and opinions of authors expressed herein do not necessarily state or reflect those of the United States Government or any agency thereof.

\*Presented at the Annual Meeting of the American Nuclear Society, Los Angeles, CA, 1982. To appear in Nuclear Technology/Fusion.

## **DISCLAIMER**

**This report was prepared as an account of work sponsored by an agency of the United States Government. Neither the United States Government nor any agency thereof, nor any of their employees, make any warranty, express or implied, or assumes any legal liability or responsibility for the accuracy, completeness, or usefulness of any information, apparatus, product, or process disclosed, or represents that its use would not infringe privately owned rights. Reference herein to any specific commercial product, process, or service by trade name, trademark, manufacturer, or otherwise does not necessarily constitute or imply its endorsement, recommendation, or favoring by the United States Government or any agency thereof. The views and opinions of authors expressed herein do not necessarily state or reflect those of the United States Government or any agency thereof.**

## **DISCLAIMER**

**Portions of this document may be illegible in electronic image products. Images are produced from the best available original document.**

## I. INTRODUCTION

The range of impurity elements found in the high-temperature plasmas of controlled fusion devices is quite broad, ranging from helium ( $Z = 2$ ) up through tungsten ( $Z = 74$ ) depending on the device in question. The understanding of impurities in these plasmas involves both atomic physics as well as plasma physics and is a critical component in the achievement of controlled fusion power. Detailed calculation of the behavior of impurity ions in fusion plasmas requires numerical solution of systems of coupled partial differential equations which describe the evolution of the impurity density in time, space, and ionization state. Several computer codes developed for impurity modeling at the Princeton Plasma Physics Laboratory will be discussed. These codes model impurity behavior in the low-density, high-temperature hydrogenic plasmas typical of magnetically confined fusion devices, such as tokamaks.

Impurity modeling codes are used in various ways in fusion research. One fundamental application involves the measurement of basic plasma parameters, such as the derivation of electron temperatures from impurity line radiation. Another important experimental application arises from the fact that much of the detailed physics of impurity behavior is still poorly understood. For example, one can use the codes to empirically determine particle transport coefficients by comparing code results with spectroscopic observation of impurity ion densities and time behavior. As our knowledge of impurity behavior improves, aided by such studies and theoretical work, then the codes can be employed with increasing confidence to model and aid in the design of future experiments, up to and including fusion power reactors.

The theoretical and experimental study of impurities in fusion plasmas is an area of active interest in the fusion community, and a wide variety of

techniques and codes have been developed. We will not attempt here a comprehensive review of these various impurity studies, or of the many computer codes currently employed in such work. Rather the physics and numerical methods involved in certain specific codes developed at the Princeton Plasma Physics Laboratory will be discussed, and examples will be presented of typical applications and results. To begin, a brief review is presented of the various roles impurities play in magnetic fusion plasmas (Section II), and the relevant atomic processes occurring in these plasmas are outlined (Section III). Local codes with zero spatial dimensions (0-D) are relatively simple and are described in Sections IV and V. A full 1-D radial transport code which treats the atomic and transport processes simultaneously for each impurity ionization state is invaluable for the more complete description of realistic plasmas and is discussed in Section VI. A summary and comments on future development directions appear in Section VII.

## II. IMPURITY EFFECTS AND DIAGNOSTIC APPLICATIONS

Some level of impurity concentration occurs naturally in all plasma devices as a result of the inevitable presence of material walls somewhere on the plasma periphery. In addition to the vacuum vessel itself, there are usually various structures within the vacuum vessel associated with coils and diagnostics. Many devices also operate with limiters specifically intended to constrain the hot plasma to some safe distance from the walls. A host of processes, such as arcing and sputtering, release impurity atoms from these material surfaces. These atoms include both those of the underlying material itself (carbon, iron, tungsten, etc.), as well as those of other elements, such as oxygen, which are bound to their surfaces. Elimination (or at least control) of these impurity sources is desirable, but difficult to achieve. In

contrast, impurity elements are sometimes deliberately introduced into the plasma. This may be done by gas puffing or by laser ablation of a thin film of material off a sample slide (1). The purpose may be to encourage certain desirable impurity effects (such as enhanced ohmic heating), or it may be related to specific diagnostics which require the controlled presence of certain impurity ions. Once an impurity is introduced, deliberately or otherwise, into the plasma periphery, its subsequent behavior and effects are governed by the atomic physics and transport phenomena it encounters, first in the scrapeoff region between the wall and limiter radius and then in the hot plasma core itself.

The presence of impurities has certain important effects on the bulk plasma parameters. First, because of their high charge, impurity ions contribute significantly to the plasma resistivity. This resistivity in turn affects both the ohmic heating rate and current profile in devices, such as tokamaks, which rely on large circulating internal plasma currents.

Radiative cooling by impurities is an effect which can range from devastating to beneficial, depending on the location and rate at which power is lost due to this process. Severe cooling of the central plasma core via line radiation from heavy metals can have catastrophic consequences (2) and has led to the removal of such materials as molybdenum and tungsten from many machines. On the other hand, radiative cooling at the plasma edge offers a relatively benign channel for heat transport from the plasma core to the walls. In principle, the plasma edge can be tailored to a desired temperature via properly controlled impurity radiation from this region.

Other impurity effects include their influence on the deposition of neutral heating beams (via beam-impurity ion collisions which ionize the beam atoms) and the dilution of a reacting plasma. Since a principal plasma

constraint is the electron density, one impurity ion effectively replaces a number of hydrogen fuel ions equal to its total charge.

Impurities can also act as valuable diagnostic tools, in part because they are a plasma constituent which is uniquely identifiable via its characteristic line radiation. Since the plasma is optically thin to this radiation, impurity ions can be studied throughout the plasma volume by spectrometry from the outside. This line radiation is often detectable from impurity concentrations sufficiently small that they are essentially non-perturbing to the bulk plasma. Most plasma devices have at least one spectrometer, and on larger machines several spectrometers covering a wide range of wavelengths are typically available.

The ionization state reached by an impurity is a strong function of the plasma electron temperature; hence, the presence or absence of line radiation from various charge states is a measure of the electron temperature. While on larger machines more accurate data is commonly available via Thompson scattering and other methods, on small devices this technique is still quite important. The electron temperature and density can also be determined from line ratios.

The doppler width of certain selected impurity ion transitions can be measured to sufficient accuracy that ion temperatures can be obtained (3). In other cases, plasma flow velocities (such as toroidal rotation in tokamaks) can be measured by the doppler shift of impurity ions moving with the bulk plasma ions.

Finally, the ability to measure in detail the spatial distribution and time evolution of impurity ion densities throughout the plasma via spectroscopy provides a unique tool for the determination of plasma particle transport and confinement. These observations can either rely on naturally

occurring impurity elements, or selected impurities can be introduced in a controlled manner in order to observe their subsequent behavior.

### III. ATOMIC PROCESSES

The high electron temperature ( $1 \text{ eV} < T_e < 100 \text{ keV}$ ) and low density ( $n_e \lesssim 10^{15} \text{ cm}^{-3}$ ) of magnetically confined fusion plasmas allows certain (coronal) approximations to be taken as a starting point when treating the atomic physics of the impurity ions. First, the plasmas are optically thin to atomic line radiation, and hence all photoabsorption processes may be neglected. We also have collision times at these low densities much longer than the decay times of most excited atomic states, with the result that each ion may be taken to be in its ground state at the start of any collisional process. Working at or near this coronal limit greatly simplifies both the atomic processes which need to be considered, as well as the formulation of the associated transport models for the impurity ions.

In the following, we will briefly note the atomic processes which must be considered in the impurity calculations. Various additional processes and considerations peculiar to the scrapeoff region of the plasma, such as molecules, will not be considered. Data on the cross sections and rate coefficients for these processes is fundamental to any impurity modeling calculations. Therefore, the calculation and measurement of such data on the part of the atomic physics community is a critical part of our increasing understanding of fusion plasma impurities. This research presents challenging problems in its own right.

Ionization of ions of an impurity element with atomic number  $Z$  and charge  $q$  is primarily due to direct electron impact ionization:



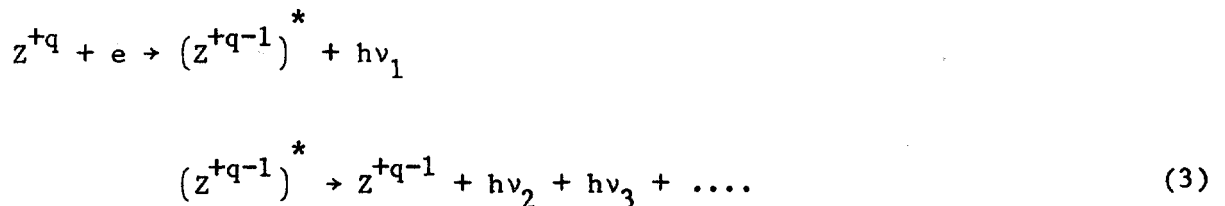


For some ions, excitation to autoionizing states may also be an important process. Here, the electron impact removes an electron indirectly by exciting the ion to a state which subsequently decays by the ejection of an electron rather than by radiation. Combining these two processes, we can define a total ionization rate per ion as

$$I_q = n_e k_q (T_e) , \quad (2)$$

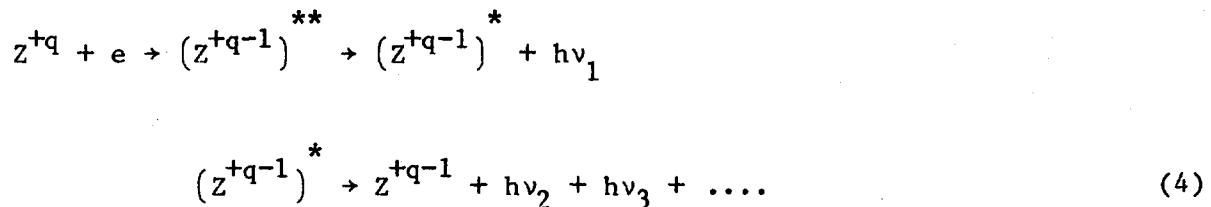
where  $T_e$  is the electron temperature,  $n_e(\text{cm}^{-3})$  is the electron density, and the ionization rate coefficient  $k_q(\text{cm}^3\text{s}^{-1})$  is essentially independent of  $n_e$ . Rate coefficients such as  $k_q$  result from the average over a maxwellian velocity distribution of the cross section - velocity product,  $\langle\sigma v\rangle$ .

For recombination of an ion, radiative, dielectronic, and charge exchange rates typically must be considered. Radiative recombination proceeds by direct capture of an electron from the continuum with the emission of one or more photons:



The second step involving decay of an excited state via line radiation occurs only if the electron was not directly captured into the ground state of the ion.

Dielectronic recombination is a complex process whereby a free electron is captured into a highly excited level of an ion during the excitation of a bound electron. This doubly excited state is unstable against autoionization, but will sometimes stabilize before this occurs by radiative decay of the inner excited electron. Cascade of the captured electron to the ground state follows, resulting in the recombined ion:



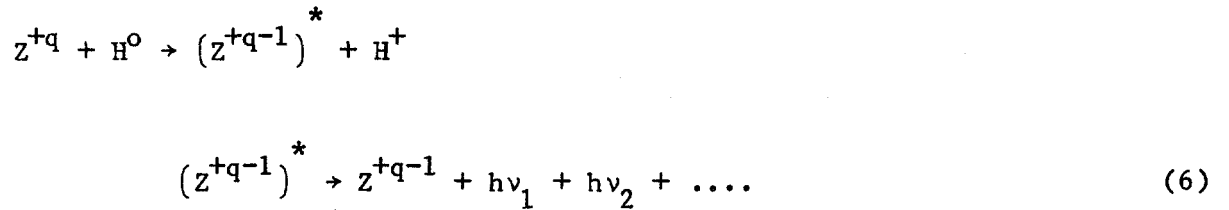
Both radiative and dielectronic recombination occur due to electron impact and, hence, can be combined into a total recombination rate per ion:

$$R_q = n_e \alpha_q \left( \frac{T_e}{e} \right), \tag{5}$$

where the total recombination rate coefficient  $\alpha_q$  ( $\text{cm}^3 \text{s}^{-1}$ ) includes both the radiative and dielectronic processes. While  $\alpha_q$  does have an intrinsic density dependence via the dielectronic process, in many cases this dependence is weak over the density range of interest in a particular problem. For present purposes,  $\alpha_q$  will therefore be written as independent of density. In general, however, this effect cannot be neglected. This is particularly true at the high density and/or low temperature extremes of the parameter ranges mentioned in the introduction to this section.

Neutral hydrogen atoms present in the plasma (produced either by charge-exchange transport of recycling plasma from the cool edge region or by neutral beam injection) can charge exchange with impurity ions and produce a

significant net recombination rate:



This rate depends on the neutral hydrogen density instead of the electron density. In order to simplify the following discussions, charge-exchange recombination will be neglected, but it is important to note that it can be an important process in certain plasmas (4).

The prime radiation mechanism for impurity ions is line radiation due to electron impact excitation followed by prompt radiative decay. Other processes of importance include line and continuum radiation associated with the recombination processes and bremsstrahlung. Neglecting charge-exchange recombination, all these processes are the result of electron impact, and, therefore, one can write a total radiation rate coefficient for each charge state  $\lambda_q(T_e)$  (watts-cm<sup>3</sup>) which is a function of the electron temperature. The radiative cooling for a given ion  $P_q$  (watts) is simply given by

$$P_q = n_e \lambda_q(T_e) \quad (7)$$

Rate coefficients for these processes have been obtained from those originally used in the average ion code of Post et al. (5) by reformulating them in terms of individual charge states. In addition, detailed spectral line excitation rates are calculated separately as required for each specific modeling application.

#### IV. CORONAL EQUILIBRIUM

Given the necessary rate coefficients from the preceding section, it is a simple matter to obtain the local (zero-dimensional), time-independent solution for the ionization balance of an impurity in equilibrium with its surrounding plasma. Since the total flow between adjacent ionization states must be zero, the densities of the individual charge states  $n_q(\text{cm}^{-3})$  are simply given by

$$\frac{n_{q+1}}{n_q} = \frac{I_q}{R_{q+1}} = \frac{k_q(T_e)}{\alpha_{q+1}(T_e)}, \quad (8)$$

taken together with the constraint that the total impurity density  $n_Z(\text{cm}^{-3})$  is given by

$$n_Z = \sum_q n_q. \quad (9)$$

Note that the resulting ionization balance is primarily a function of the electron temperature,  $T_e$ , with the only density dependence occurring via the dielectronic recombination rate as previously discussed. This "coronal equilibrium" result is often used as a starting point for understanding impurity effects in plasmas. The associated total radiated power  $P(\text{watts cm}^{-3})$  can be simply calculated from

$$P = \sum_q n_e n_q \lambda_q(T_e) = n_e n_Z \lambda_Z^{\text{CE}}(T_e). \quad (10)$$

The coronal equilibrium radiation rate (cooling rate) coefficient  $\lambda_Z^{\text{CE}}(T_e)$  and charge state fractions  $f_q^{\text{CE}}(T_e)$

$$\lambda_Z^{\text{CE}}(T_e) = \sum_q f_q^{\text{CE}}(T_e) \lambda_q(T_e)$$

$$f_q^{\text{CE}}(T_e) = \frac{n_q}{n_Z} \Big|_{\text{CE}}, \quad (11)$$

are tabulated in the literature for various elements (5,6).

Figure 1 shows the coronal equilibrium ionization balance and radiation rate coefficient for iron as a function of electron temperature for  $10 \text{ eV} < T_e < 10 \text{ keV}$ . Note the persistence of  $\text{Fe}^{+16}$  and  $\text{Fe}^{+24}$ , which correspond to the relatively stable closed-shell neon-like and helium-like states. This sort of shell structure is evident in corresponding curves for all elements. In particular, the helium-like, hydrogen-like, and fully-stripped ions radiate relatively poorly, and hence it is possible to "burn out" impurities to reduce their cooling effect.

The inclusion of charge-exchange recombination introduces a dependence on the neutral hydrogen density into these calculations and thereby complicates the corresponding results. A given neutral hydrogen velocity spectrum results in a family of ionization balance and total radiation curves which are parameterized by the neutral fraction,  $(n_H/n_e)$  (4).

Assuming local coronal equilibrium is an adequate approximation when the plasma is stable in time, and the impurity particle transport across inhomogeneities in the plasma is slow compared with the ionization and recombination times.

## V. ZERO-DIMENSIONAL TIME-DEPENDENT MODEL

When coronal equilibrium is a poor approximation, one may introduce a time-dependent, zero-dimensional calculation. Here we need to solve the

coupled rate equations:

$$\frac{\partial n_q}{\partial t} = I_{q-1} n_{q-1} - (I_q + R_q) n_q + R_{q+1} n_{q+1} - \frac{n_q}{\tau_q} + S_q . \quad (12)$$

The ionization and recombination rates  $I_q$  and  $R_q$  now may vary with time in response to the changing electron temperature and density of the impurity ion's environment. The  $\tau_q$  decay times and  $S_q$  source/sink terms can also be arbitrary functions of time.

The set of coupled equations (12) of such a zero-dimensional impurity model are readily transformed into an implicit finite-difference scheme for numerical solution (7). Here "zero-dimensional" refers to the zero spatial dimensions of the model; the multi-species (e.g., multi-ionization state) codes described here always have the additional charge state dimension to solve in beyond the number of spatial dimensions considered. Since the charge-state dimension is already intrinsically discrete, however, finite differences need only be taken in the time and spatial coordinates (if any).

Equation (12) becomes in vector form

$$\frac{\vec{n}' - \vec{n}}{\Delta t} = \tilde{A} \cdot ((1 - \theta) \vec{n} + \theta \vec{n}') + \vec{S} , \quad (13)$$

where

$$\vec{n} = \begin{pmatrix} n_0 \\ n_1 \\ n_2 \\ \vdots \\ n_Z \end{pmatrix} \text{ and } \vec{S} = \begin{pmatrix} S_0 \\ S_1 \\ S_2 \\ \vdots \\ S_Z \end{pmatrix} . \quad (14)$$

The  $(Z + 1) \times (Z + 1)$  matrix  $\tilde{A}$  contains the ionization and recombination rates and the  $\tau_q$  term. The implicitness factor  $\theta$  may be adjusted from

$\theta = 0$  (fully explicit) to  $\theta = 1$  (fully implicit) although  $\theta \geq 0.5$  is dictated for stability. This equation advances the system to a new state  $\vec{n}'$  a timestep of length  $\Delta t$  advanced from the state  $\vec{n}$ .

Equation (13) is trivially put in the form

$$\tilde{X} \vec{n}' = \vec{y}, \quad (15)$$

where  $\tilde{X}$  and  $\vec{y}$  are known.  $\tilde{X}$  is tri-diagonal (as is  $\tilde{X}$ ) since the atomic processes connect only adjacent ionization states. The solution is thus easily obtained (7) by elimination on  $\tilde{X}$  by assuming solutions of the form

$$n'_q = E_{q-1} n'_{q-1} + F_{q-1}. \quad (16)$$

When (16) is substituted into (15), one obtains recursive relations for  $E_q$  and  $F_q$  which involve  $E_{q+1}$  and  $F_{q+1}$  plus the known elements of  $\tilde{X}$  and  $\vec{y}$ . One then starts by evaluating these recursion relations at  $q = Z$  and sweeps down to  $E_0$  and  $F_0$ . The  $n'_q$  are then extracted from (16) on a return sweep from  $q = 0$  to  $q = Z$ . The boundary conditions are invoked at the endpoints, and simply reflect the absence of  $n_{-1}$  and  $n_{Z+1}$ . This procedure is quickly carried through on even a small computer, which makes such codes of great practical utility.

Beyond the algorithm described above, one must supply a choice of  $\Delta t$  for each timestep. This is done dynamically in the code by establishing some index of how rapidly the system is changing in time. A useful particular choice is

$$\delta = (\Delta n_q)_{\max} / (n_q)_{\max}, \quad (17)$$

where  $(\Delta n_q)_{\max}$  is the largest change in any ionization state density during the last timestep and  $(n_q)_{\max}$  is the largest density. This choice discounts fast changes in ionization states which have negligible densities. This change parameter  $\delta$  is compared after each timestep with a specified  $\epsilon$ , which is the target change per timestep. The code then adjusts the next timestep length in such a way (either longer or shorter) as to try to approach this target. This system works quite well for most applications.

With fixed plasma parameters and no source/sink terms, these equations, of course, yield ionization balances and radiative cooling rates which converge towards coronal equilibrium from any given initial state. But in many cases, the finite rate at which the impurity can respond to rapid changes in its environment lead to important departures from coronal equilibrium. In the case shown in Fig. 2, a cold plasma containing an initially neutral oxygen impurity has been instantaneously heated to an electron temperature of 50 eV. The electron density is taken to be  $n_e = 2 \times 10^{14} \text{ cm}^{-3}$ . This is a representative situation for many small plasma devices, such as spheromaks, which heat on time scales fast compared with characteristic ionization times for their intrinsic impurities. In Fig. 2(a), the fractional distribution of the oxygen impurity among its different ionization states is shown as a function of time. The final coronal equilibrium distribution is not approached for several hundred microseconds, which is often much longer than the plasma lifetimes in such machines. One result of this is that the use of ionization balances observed spectroscopically in such situations will yield incorrect estimates for the electron temperature if simple coronal equilibrium is assumed.

Figure 2b illustrates another consequence of the non-equilibrium nature of the oxygen distribution. The effective radiative cooling coefficient of



the oxygen is well above that which would obtain in coronal equilibrium at 50 eV as a consequence of the finite time required for the oxygen to burn out to the relatively non-radiative helium-like state. Until this occurs, the oxygen radiates quite strongly, with an integrated energy loss which can be many keV per oxygen ion. This radiative energy loss often cannot be sustained by the heating in small devices and produces the phenomenon often referred to as the "oxygen barrier." Other elements (such as carbon) can produce similar effects.

Zero-dimensional time-dependent codes can also be used to obtain initial approximations to situations where transport of the impurity is the important process keeping the ions away from coronal equilibrium. For example, one may consider a homogeneous volume which is kept from coronal equilibrium by finite source and sink terms. The particular situation where impurities recycle as neutrals back into the plasma after being transported out as ions can be modeled by setting up a finite source of neutral atoms in the  $S_0$  term of equation (12), and then setting a finite confinement time  $\tau_q$  for all the other charge states.

One can also attempt to mock up one-dimensional spatial transport using a zero-dimensional code by choosing some velocity with which a test packet of impurity is moved through a fixed plasma profile, such as that shown in Fig. 3. The time varying  $T_e$  and  $n_e$  seen by the impurity thus reflect its changing position in the plasma. An approximate departure from coronal equilibrium to be expected from impurities transporting through a plasma can be quickly calculated using this approach. However, the uniform convective motion assumed for the impurity ions in this model cannot directly include a diffusive "random walk" component in the impurity transport. Since diffusion is likely to be important in most situations, some uncertainty arises in the

interpretation of results from such models.

## VI. ONE-DIMENSIONAL RADIAL TRANSPORT

### VI.A. Equations and Numerical Solution

Computer models which treat impurity transport and the atomic processes of ionization and recombination simultaneously and self-consistently are necessary to treat accurately the many situations in which these processes occur on comparable time scales. Full three-dimensional solutions for impurity behavior are unnecessary as most plasmas have some degree of symmetry which can be exploited. The 1-D model to be presented here was written primarily for application to tokamak plasmas. In a tokamak, particle motion in the poloidal and toroidal directions occurs along field lines and, thus, is typically quite fast compared with cross-field radial motion. Assuming symmetry in all but the radial coordinate (cylindrical geometry) is thus a physically reasonable choice for a model, resulting in a one-dimensional impurity transport code.

The expression governing the time evolution of a given impurity charge state density in space and time now has the form

$$\frac{\partial n_q}{\partial t} = -\frac{1}{r} \frac{\partial}{\partial r} (r \Gamma_q) + I_{q-1} n_{q-1} - (I_q + R_q) n_q + R_{q+1} n_{q+1} - \frac{n_q}{\tau_q} + S_q, \quad (18)$$

where we have introduced a particle flux density  $\Gamma_q$ . This flux is taken to be of the general form

$$\Gamma_q = -D_q(r) \frac{\partial n_q}{\partial r} + v_q(r) n_q, \quad (19)$$

where  $D_q(r)$  is the particle diffusion coefficient, and  $v_q(r)$  is a convective velocity. These transport coefficients may, as indicated, be functions of the ionic charge as well as space and time. Similarly, the  $I_q$ ,  $R_q$ ,  $\tau_q$ , and  $S_q$  are functions of charge state, radius, and time. As will be described later, the  $n_q/\tau_q$  and  $S_q$  terms are primarily used to model impurity ion loss, recycling, and deposition in the plasma scrapeoff region near the wall.

For tokamaks, neoclassical transport theory provides expressions for  $D_q(r)$  and  $v_q(r)$ . These neoclassical transport coefficients depend on the temperature and density profiles of the background hydrogenic ions (8). There are also contributions from ions of other impurity elements and ions of the same element in different charge states. In most tokamak plasmas, however, it appears that anomalous processes either add to or completely dominate neoclassical transport. In order to handle such cases, the code allows for arbitrary values of the transport coefficients to be specified. These may be chosen either to correspond to some alternative transport model, or they may be adjusted to yield a match between the code results and experimental data.

Numerical solution of the set of coupled equations (18) is undertaken using an implicit scheme similar to that used for the 0-D code. A radial mesh is specified and the finite differences are taken in  $r$  and  $t$ . The charge-state dimension is, as before, already in a discrete form. Conservative differencing is used in the radial coordinate to ensure particle conservation to within the machine accuracy. In each radial zone  $1 < j < N_{\text{zones}}$ , we have a vector  $\vec{n}_j$  containing the  $Z + 1$  charge-state densities  $n_q$ . The implicit finite differencing yields a result similar in overall form to that of the 0-D equation:

$$\tilde{\chi} \cdot \vec{\eta}' = \vec{\gamma} . \quad (20)$$

The  $\vec{\eta}'$  vector here has the dimension of the number of radial zones  $N_{\text{zones}}$  and has, as its elements, the charge-state vectors  $\vec{n}'_j$  each  $(Z + 1)$  long. Correspondingly,  $\tilde{\chi}$  is now a  $(N_{\text{zones}}) \times (N_{\text{zones}})$  matrix whose elements are  $(Z + 1) \times (Z + 1)$  matrices. The  $\tilde{\chi}$  matrix is tri-diagonal, this time because the second order difference operator only connects a given radial zone to its adjacent zones. Therefore, one can straightforwardly apply the same tri-diagonal elimination scheme as before except now the sweeps are in radial zone space. The substitution,

$$\vec{n}'_j = \tilde{E}_{j-1} \vec{n}'_{j-1} + \vec{F}_{j-1} , \quad (21)$$

results in recursion relations for the  $\tilde{E}_j$  and  $\vec{F}_j$  which involve  $(Z + 1) \times (Z + 1)$  matrices. These matrix equations are solved using a standard Gaussian elimination technique with pivoting (9).

The radial boundary conditions are applied at the inner and outer limits of the radial mesh during the tri-diagonal matrix sweeps. Flux or density conditions may be imposed at each boundary, with the usual choices being a zero flux on axis ( $r=0$ ) and a zero density at the plasma edge. The latter boundary condition is somewhat unphysical, but the scrapeoff model discussed below naturally produces small densities in the edge zones so the boundary condition there is not critical.

Since the impurity transport coefficients are explicitly rather than implicitly defined functions of the plasma parameters, the code also contains a predictor-corrector loop to improve stability in situations where these

transport coefficients are sensitive functions of the changing impurity densities. For example, this can occur when the impurity ion-impurity ion transport terms in neoclassical theory become important.

In addition to the numerical algorithm just described, the 1-D code also carries out various auxiliary calculations as part of the physical model. Several of these concern physics associated with the wall and scrapeoff region of the plasma. The detailed physics of impurity behavior in the scrapeoff region of a plasma is a complex topic in itself. Since the main applications of this code are currently associated with impurity transport and effects in the central plasma core region, a fully detailed scrapeoff model has not been incorporated. However, some of the essential features are modeled in order to provide suitable source and sink terms in this region.

Beyond a specified radius in the model, the finite confinement time term  $(-n / \tau_q)$  is employed to simulate loss of impurity ions along the field lines which either strike the limiter or connect to a divertor region (10). The appropriate parallel loss time is either calculated using a ratio of a toroidal connection length to the ion sound speed, or may be specified externally if desired. Impurities lost via this parallel loss term and by cross-field transport to the wall can be recycled into the plasma in various ways. One of these is to return the lost impurity ions as neutral atoms of some given energy launched from the wall. The deposition profile of these neutrals is calculated to yield a radially dependent source of singly charged impurity ions which typically peaks in the scrapeoff region. The ratio between the instantaneous magnitude of the entering neutral particle source and the total scrapeoff and wall loss rate is the recycling coefficient. This quantity is specified as somewhere between zero and one-hundred percent depending on the element and problem in question. For injection experiments

where an instantaneous puff of impurity is introduced into the plasma periphery, the same type of deposition calculation is used to initialize the problem with a given initial distribution, rather than continuous source, of singly ionized impurity ions.

Despite the  $(Z + 1) \times (Z + 1)$  matrices which must be handled by this algorithm, total computing time for typical problems is reasonable on a fast scientific computer such as the CRAY-1. This is partly because the matrix manipulations vectorize quite efficiently on a machine such as this. A factor of  $\sim 10$  improvement in speed was achieved on the CRAY-1 relative to the CDC-7600 without resorting to any special coding techniques. Exact execution times depend strongly on the particular element  $(Z)$  and problem being run. Typical runs on the CRAY-1 take anywhere from seconds for low- $Z$ , transport equilibrium cases up to tens of minutes for detailed, high- $Z$ , impurity injection models. Equation (18) is particularly stiff in the edge region where the impurity neutrals are typically introduced, and special solution techniques may be needed in the future to yield efficient execution times when this region is considered in more detail.

Real tokamaks are, of course, never perfectly symmetric in the poloidal and toroidal coordinates, and there are certain circumstances in which these asymmetries may become important. An interesting example of this involves neutral beam injection, which produces toroidally asymmetric charge-exchange recombination of the impurity ions. A one-dimensional transport code which considers toroidal rather than radial transport was written in order to handle this situation (11). Poloidal asymmetry due to the localized nature of impurity sources (such as limiters) and other causes is also frequently observed in the outer regions of tokamak plasmas, but it usually decreases as one proceeds further into the plasma core.

Despite these last caveats, one-dimensional radial impurity transport models handle most problems of current interest and can be calculated with a reasonable expenditure of computer effort.

#### VI.B. Applications and Examples

In order to demonstrate some of the typical applications of the 1-D multi-species impurity transport code, the plasma profiles shown in Fig. 3 will be used. Such a plasma is representative of those which may be obtained in present large tokamaks. The scrapeoff region extends from the  $r = 40$  cm limiter radius out to the wall at  $r = 50$  cm.

Perhaps the simplest calculation which can be performed using the 1-D impurity transport code involves the effect of transport on the steady-state ( $\partial n_q / \partial t = 0$ ) distribution of a naturally occurring impurity. In the absence of transport, this steady-state solution corresponds to achieving local coronal equilibrium everywhere. No recycling is needed since the impurity ions do not move and are not lost from the plasma. In Figure 4a, such a solution is shown for an iron impurity with constant density  $n_{Fe} = 1 \times 10^{11}$   $\text{cm}^{-3}$  in the plasma of Fig. 3. The resulting distribution of charge states with radius is simply a mapping of the coronal equilibrium curves of Fig. 1a across radius according to the specified radial temperature profile.

In Figure 4b, a steady-state solution is shown where a radially constant diffusion coefficient  $D = 1 \times 10^4 \text{cm}^2 \text{s}^{-1}$  has been included. Diffusion coefficients of this order are inferred from various experiments (12). The recycling coefficient is one hundred percent for this problem, as it must be for a steady state to be reached in the presence of transport. The impurity outflux is recycled as neutrals at 1 eV energy as previously described. The

source and sink terms all occur in the scrapeoff outside of  $r = 40$  cm, and, as a result, the total iron density in the  $r < 40$  cm region shown is radially constant in steady state due to the purely diffusive transport. Including a convective velocity term ( $vn_q$ ) in the transport flux would give rise to radially peaked total impurity density profiles in steady state.

The total iron density in Fig. 4b has been adjusted to be the same as for the coronal equilibrium case of Fig. 4a. However, note the change of vertical scales between the two graphs necessary to show detail in the diffusive case where the individual charge-state profiles are much broader, and hence smaller in peak density. The comparison of these two cases illustrates how one can, in principle, determine impurity transport coefficients via observation of the radial profiles of impurity ions. Code calculations, such as those shown in Fig. 4, are made and the transport coefficients are adjusted until a match is achieved within the experimental uncertainties. In practice, however, often these experimental and other uncertainties (such as in the assumed temperature and density profiles, and in the atomic rate coefficients) make accurate transport assessment from this type of equilibrium data difficult.

In Figure 5, the radiative cooling rates corresponding to the steady-state solutions of Fig. 4 are shown. The transport of relatively radiative lower charge states to the plasma core in place of the less radiative helium-like state dominant in coronal equilibrium has a marked effect. One may also note here the tendency of the cooling rate to peak somewhere in the outer regions of the plasma. As previously noted, such a radiative "shell" is found in various plasmas and can sometimes be beneficial by cooling the plasma edge and, hence, reducing the severity of plasma/wall interaction effects.

In Figure 6, we show code calculations for the injection of iron into the same plasma considered in Figs. 3,4,5. Such experiments often allow



measurement of impurity transport coefficients more straightforwardly and accurately than can typically be achieved by using the steady-state observations just discussed. While iron was chosen for this example for consistency with the other cases shown, typically in an experiment of this kind one chooses an element not naturally found in the device so that there will be no confusion between the injected and background impurities. One also typically chooses an impurity which will not recycle from the walls, and hence, in this set of calculations, we have chosen the recycling coefficient to be zero.

The transport here has again been chosen to be  $D = 1 \times 10^4 \text{ cm}^2 \text{ s}^{-1}$ . The radial scale of Fig. 6 extends out to the  $r = 50$  cm wall radius in order to show the initial distribution profile and subsequent evolution in the scrapeoff region. A fixed scrapeoff loss time of  $\tau = 0.5$  ms has been taken for the  $r > 40$  cm scrapeoff region.

Note that the density axis has been rescaled for each of the four selected times shown in Fig. 6. The total impurity content of the plasma is a monotonically decreasing function of time as a result of scrapeoff and wall losses with no recycling, and the dynamic range in densities is large.

The initial distribution of singly charged iron from the injection is seen in Fig. 6a, peaked at  $r \sim 45$  cm. The total number of injected atoms is  $10^{17}$ , a typical number using the laser ablation technique.

By  $t = 3.2$  ms (Fig. 6b), several scrapeoff confinement times have passed, and the density in the scrapeoff region is nearly zero. However, in the short period before this occurred, some of the ions have had time to diffuse into the main plasma region inside of  $r = 40$  cm. Some of these ions will diffuse inward towards the center of the plasma column, while others will diffuse back out into the scrapeoff and be lost. Note the evolution of the iron in charge

state as particles flow into the hotter central region of the plasma.

By  $t = 16.6$  ms (Fig. 6c), the impurity ions have reached the center of the plasma. At long times ( $t = 60.9$  ms, Fig. 6d), the impurity has settled down to a centrally peaked radial distribution which decays exponentially in time.

As seen from study of Fig. 6, each individual charge state of the iron impurity appears, peaks, and then diminishes with time. The time of appearance and decay of each charge state is a result of the detailed interaction of the transport of the impurity through the  $T_e$  and  $n_e$  profiles and the corresponding changes in the ionization and recombination rates of the different charge states. Since the temperature profile is peaked on axis and the impurity is introduced on the periphery of the plasma, successively higher charge states appear in order as the ions move inward into the hotter central region of the plasma. One way of clearly presenting this effect is to look at the radially integrated column densities of the charge states as functions of time. This is shown in Fig. 7. Experimentally, it is straightforward to observe the time evolution of the spectral line brightness from different charge states, a quantity which is closely related to these column densities. The code calculates a quantitative spectral line brightness at a particular selected wavelength for each charge state in addition to this column density in order to allow direct comparison of code results with experimental data. Such comparisons allow the impurity transport to be deduced. Despite the recurrence of many of the same uncertainties (electron temperature, atomic rate coefficients, etc.) associated with the steady-state radial profile method, such modeling of injection data provides complimentary and sometimes superior results.

## VII. SUMMARY AND FUTURE DIRECTIONS

Impurity physics is an important part of controlled fusion research, and numerical models of impurity behavior in realistic plasmas are an important tool in the successful development of controlled fusion energy. Impurity modeling computer codes are useful both in the diagnostic measurement of plasma parameters and also in investigations of basic physics issues, such as particle transport and confinement. The codes are also invaluable in their ability to predict impurity effects, such as radiative cooling, and thereby have an important role in the design of future plasma devices, including reactors. Active research efforts concerning all these issues are in progress at various fusion laboratories. A particularly important and complex problem not treated here concerns the detailed physics of impurities in both limiter and divertor scrapeoff plasmas. Reactor design calculations have investigated the possibility of forming a radiatively cooled outer plasma region which will actively help in the removal of heat and particles from a reacting plasma.

At the present time, the predictive modeling of impurity behavior in reactor-size devices is hampered by remaining uncertainties in our understanding of impurity transport and other fundamental physics issues. Much of the current modeling efforts are thus oriented towards obtaining further data on the physics of impurities in realistic fusion plasmas. In the next few years, improved understanding and modeling of impurity transport, scrapeoff physics, and plasma/wall interactions may allow all these aspects of the problem to be brought together in a comprehensive, self-consistent model of impurity behavior. The known presence of toroidal and poloidal asymmetry, particularly in the edge and scrapeoff regions of tokamak plasmas, will probably require such a code to be extended beyond one spatial dimension. This development, especially when taken together with the interest in higher Z

elements as plasma temperatures increase, may dictate fundamental changes in the numerical algorithms employed so as to keep the computational requirements within reasonable bounds.

#### ACKNOWLEDGMENTS

The author gratefully acknowledges many useful discussions with colleagues both at Princeton and elsewhere during the development of the computer codes described here. In particular, code development advice provided by D. Post and continuing collaborations with members of the experimental division at PPPL have proved most important to this work.

This work was supported by the U. S. Department of Energy Contract No. DE-AC02-76-CHO-3073.

REFERENCES

1. E. S. MARMAR, J. L. CECCHI, and S. A. COHEN, "System for Rapid Injection of Metal Atoms into Plasmas," Rev. Sci. Instrum. 46, 1149 (1975).
2. E. HINNOV, K. BOL, D. DIMOCK, R. J. HAWRYLUK, D. JOHNSON, M. MATTIOLI, E. MERSERVY, S. VON GOELER, "Effects of Tungsten Radiation on the Behavior of PLT Tokamak Discharges," Nuclear Fusion 18, 1305 (1978).
3. S. SUCKEWER and E. HINNOV "Observation of a Forbidden Line of FeXX and Its Application for Ion Temperature Measurements in the PLT Tokamak," Phys. Rev. Lett. 41, 756 (1978).
4. R. A. HULSE, D. E. POST, and D. R. MIKKELSEN, "Charge Exchange as a Recombination Mechanism in High-Temperature Plasmas," J. Phys. B. 13, 3895 (1980).
5. D. E. POST, R. V. JENSEN, C. B. TARTER, W. H. GRASBERGER, and W. A. LOKKE, "Steady-State Radiative Cooling Rates for Low-Density, High-Temperature Plasma," Atomic Data and Nuclear Data Tables 20, 397 (1977).
6. C. BRETON, C. DE MICHELIS, and M. MATTIOLI, "Ionization Equilibrium and Radiative Cooling of a High-Temperature Plasma," J. Quant. Spectrosc. Radiat. Transfer 19, 367 (1978).
7. D. POTTER, "Computational Physics," Wiley and Sons, New York, NY (1973).

8. P. H. RUTHERFORD, S. P. HIRSHMAN, R. JENSEN, D. E. POST, F. G. P. SEIDL, "Proceedings of the International Symposium on Plasma-Wall Interactions," (Julich, FRG, October 1976) Pergamon Press for the Commission of European Communities, Oxford (1977) p. 173.

9. G. FORSYTHE and C. B. MOLER, "Computer Solution of Linear Algebraic Systems," Prentice-Hall (1967).

10. R. J. HAWRYLUK, S. SUCKEWER, and S. P. HIRSCHMAN "Low-Z Impurity Transport in Tokamaks," Nuclear Fusion 19, 607 (1979).

11. W. H. M. CLARK, J. G. CORDEY, M. COX, S. J. FIELDING, R. D. GILL, R. A. HULSE, P. C. JOHNSON, J. W. M. PAUL, N. J. PEACOCK, B. A. POWELL, M. F. STAMP, and D. F. H. START, "Impurity Radiation in DITE During Neutral Injection," Nuclear Fusion 22, 333 (1982).

12. R. HULSE, K. BRAU, J. CECCHI, S. COHEN, M. FINKENTHAL, R. FONCK, D. MANOS, and S. SUCKEWER, "The Transport of Injected Impurities in the PDX Tokamak," Bull. Am. Phys. Soc. 26, 864 (1981).

FIGURE CAPTIONS

Fig. 1. The (a) charge-state distribution and (b) radiative cooling rate coefficient for iron in coronal equilibrium from  $10 \text{ eV} < T_e < 10 \text{ keV}$ .

Fig. 2. Zero-dimensional time-dependent code solution for the behavior of an oxygen impurity taken as neutral at  $t = 0$  in a  $T_e = 50 \text{ eV}$ ,  $n_e = 2 \times 10^{14} \text{ cm}^{-3}$  plasma. The time evolution of (a) the charge-state distribution and (b) the radiative cooling rate coefficient are shown.

Fig. 3. Typical tokamak electron temperature ( $T_e$ ) and density ( $n_e$ ) radial profiles.

Fig. 4. One-dimensional transport code steady-state radial charge state density profiles for iron impurity in the plasma of Fig. (3) for (a) coronal equilibrium and (b)  $D = 1 \times 10^4 \text{ cm}^2/\text{s}$ . The total iron density in both cases is  $n_{\text{Fe}} = 1 \times 10^{11} \text{ cm}^{-3}$ . Note that the density scales for the two cases are different.

Fig. 5. The radiative cooling rate ( $\text{watts/cm}^3$ ) corresponding to the steady-state results of Fig. 4.

Fig. 6. A sequence of four radial charge-state distributions for  $10^{17}$  neutral iron impurity atoms injected into the plasma of Fig. 3 at  $t = 0$ . The scrapeoff region extends from  $r = 40 \text{ cm}$  to  $r = 50 \text{ cm}$ . Note that the density axis is rescaled as time progresses.

Fig. 7. Radially integrated column densities for selected charge states from the Fig. 6 simulation. The peak for each charge state has been normalized to unity.



#82P0146

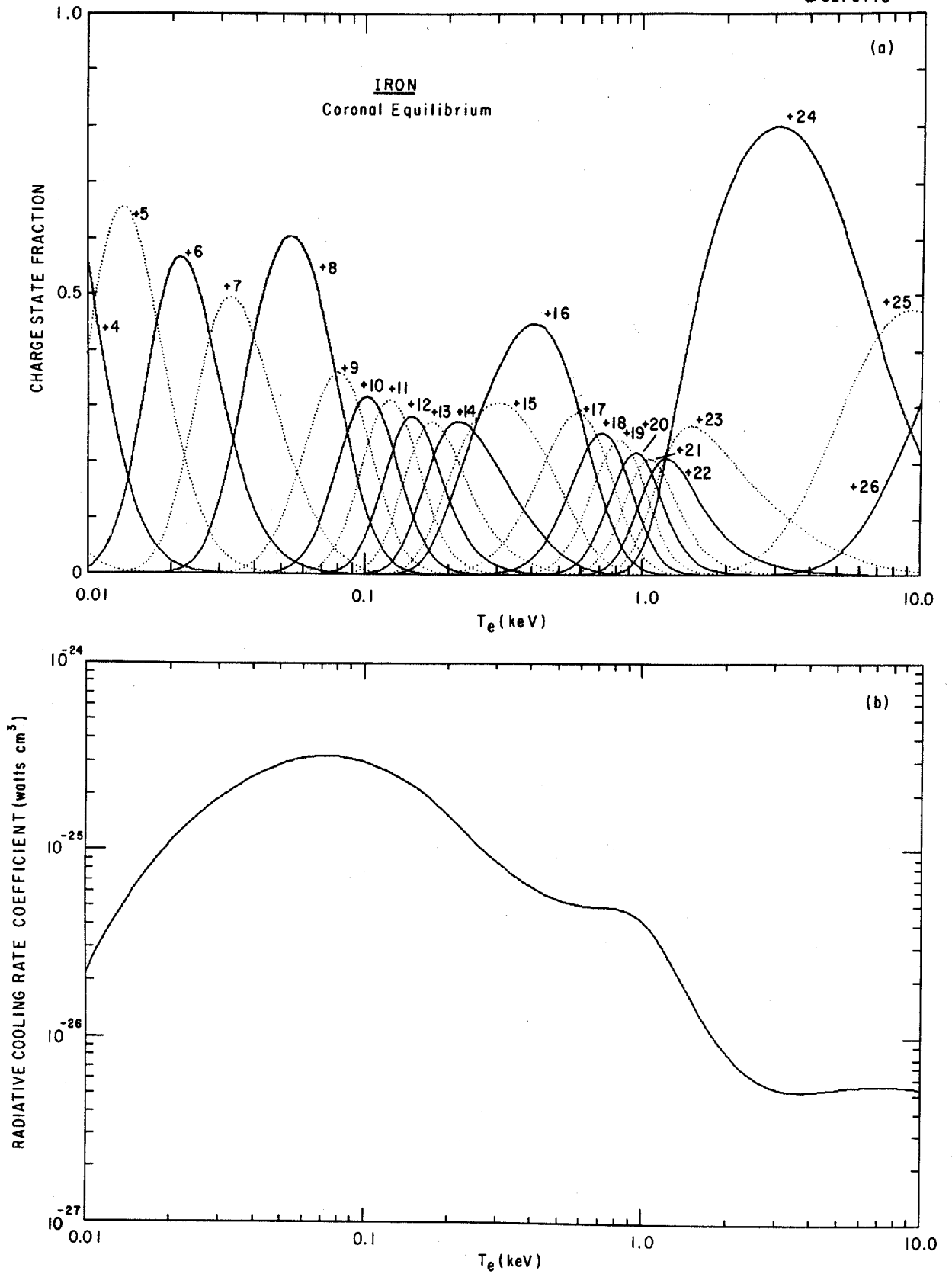


FIG. 1

#82P0143

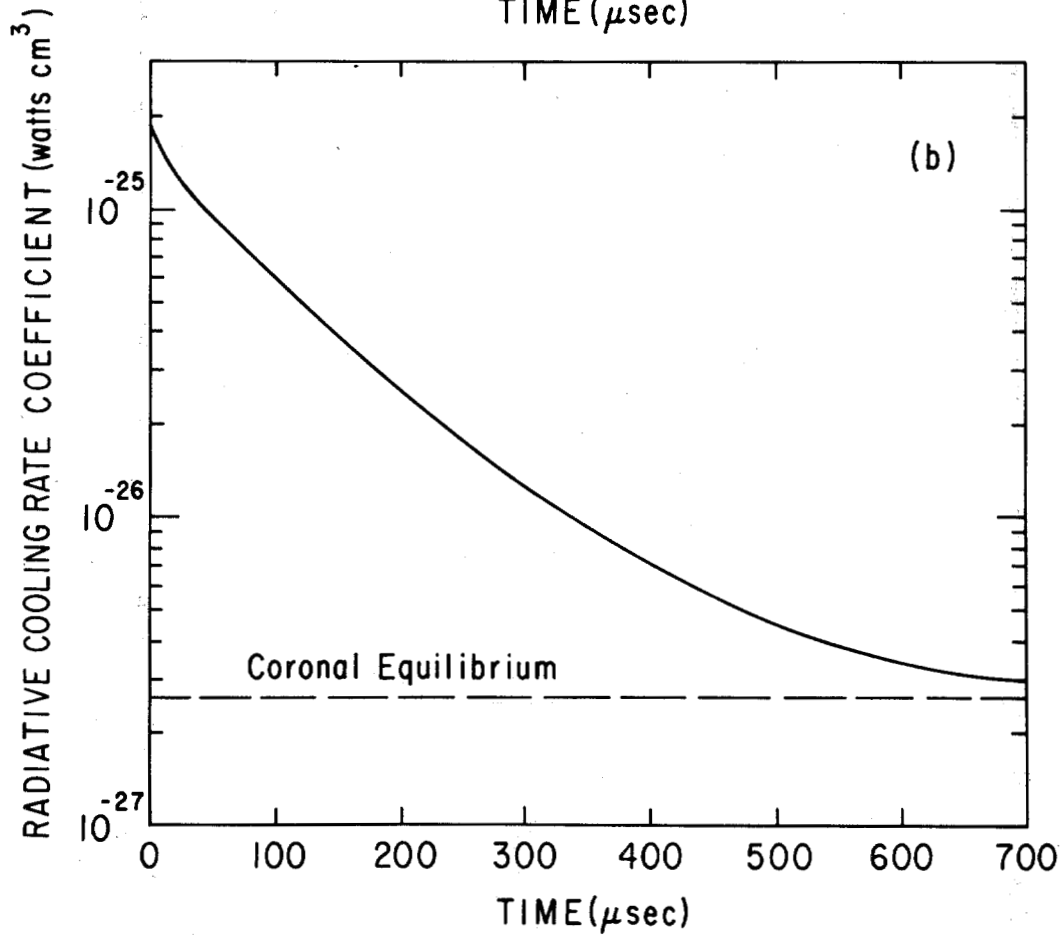
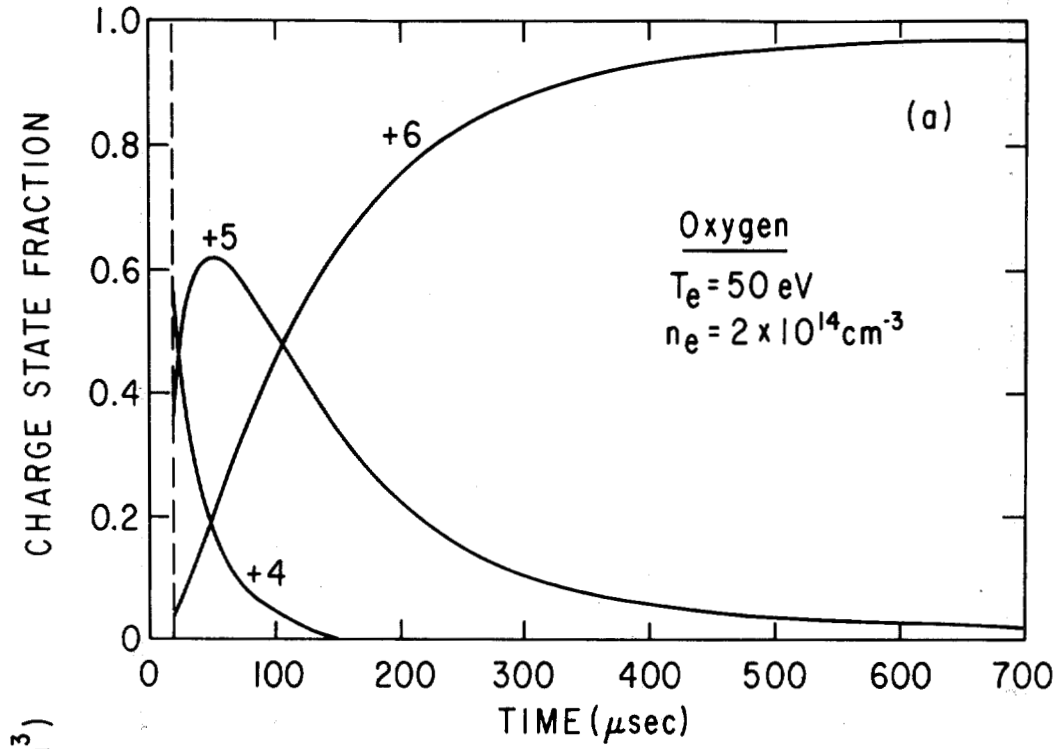


FIG. 2

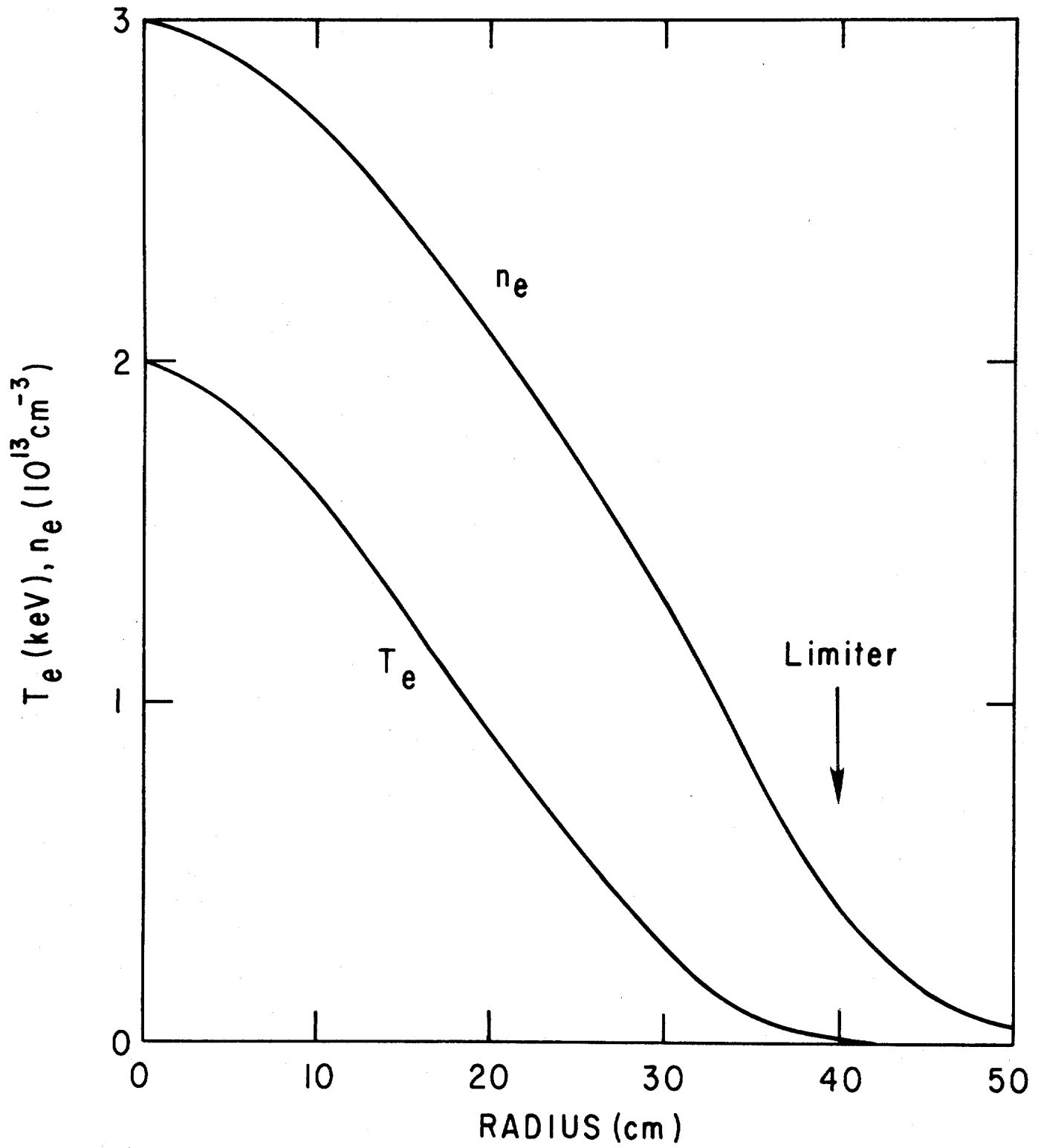


FIG. 3

#82P0145

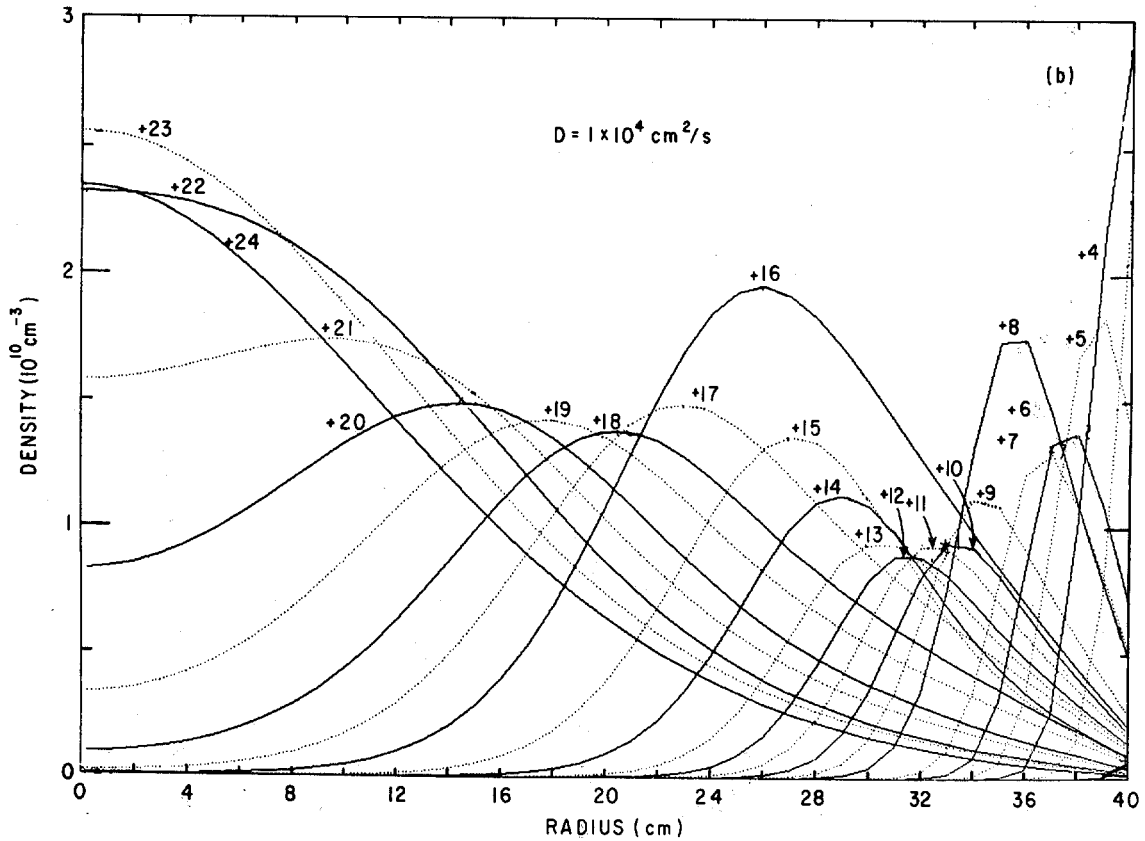
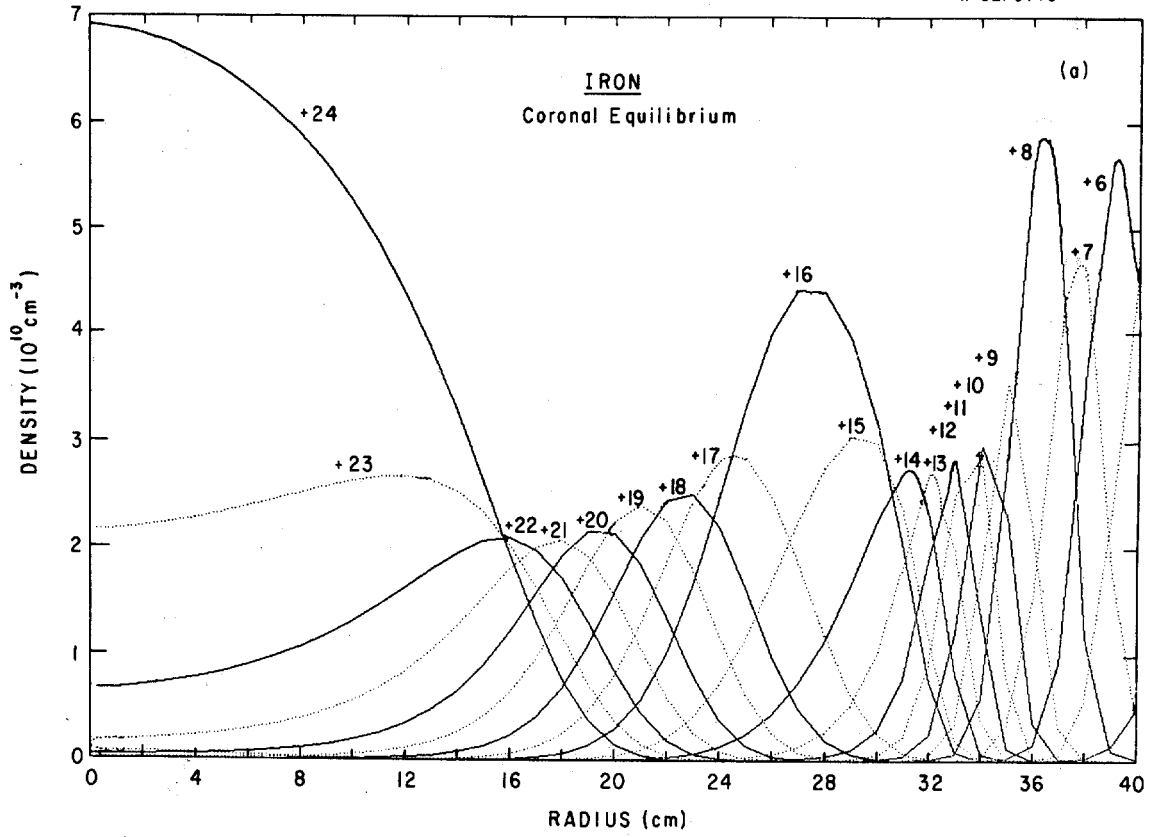


FIG. 4

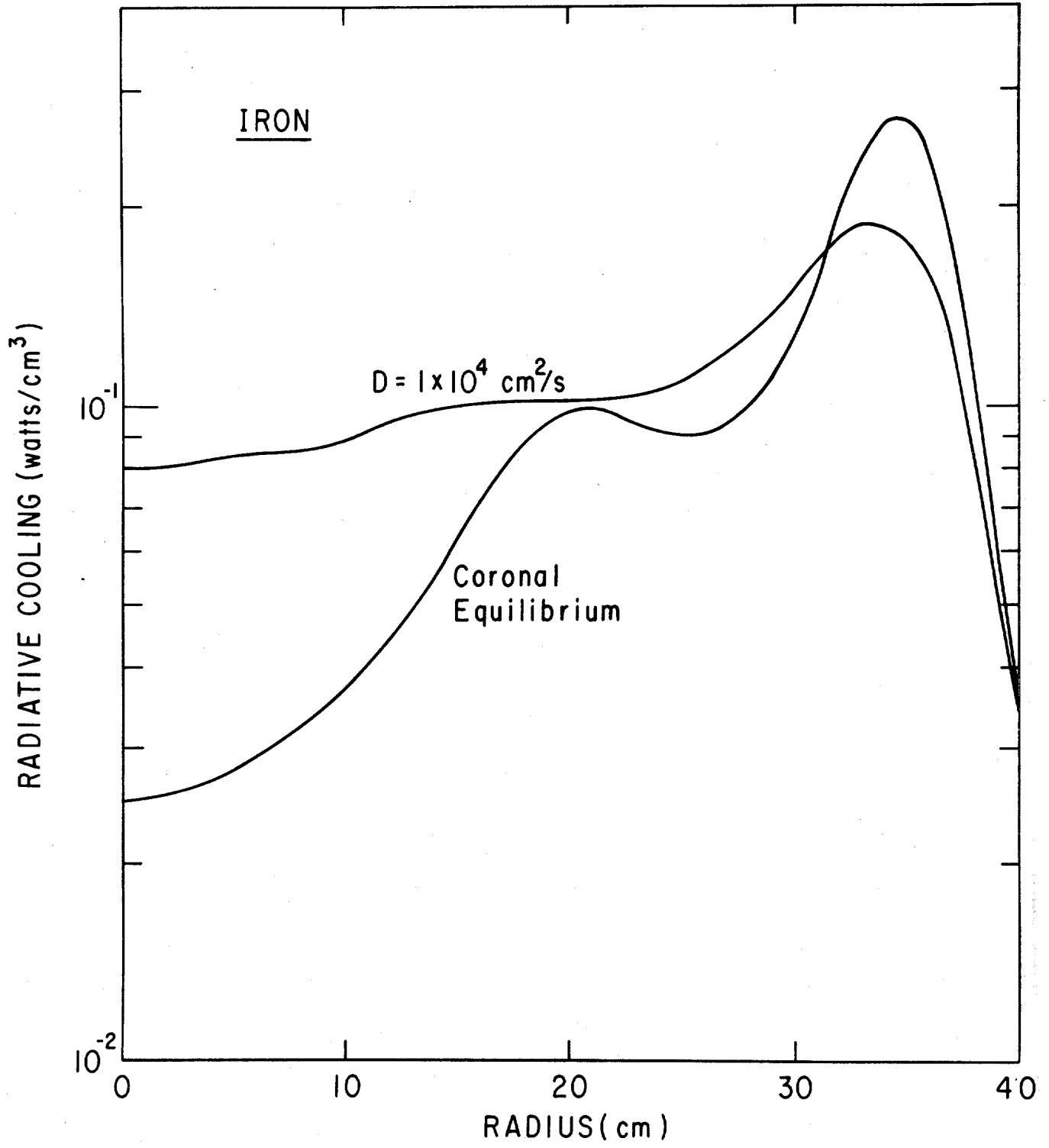


FIG. 5

#82P0147

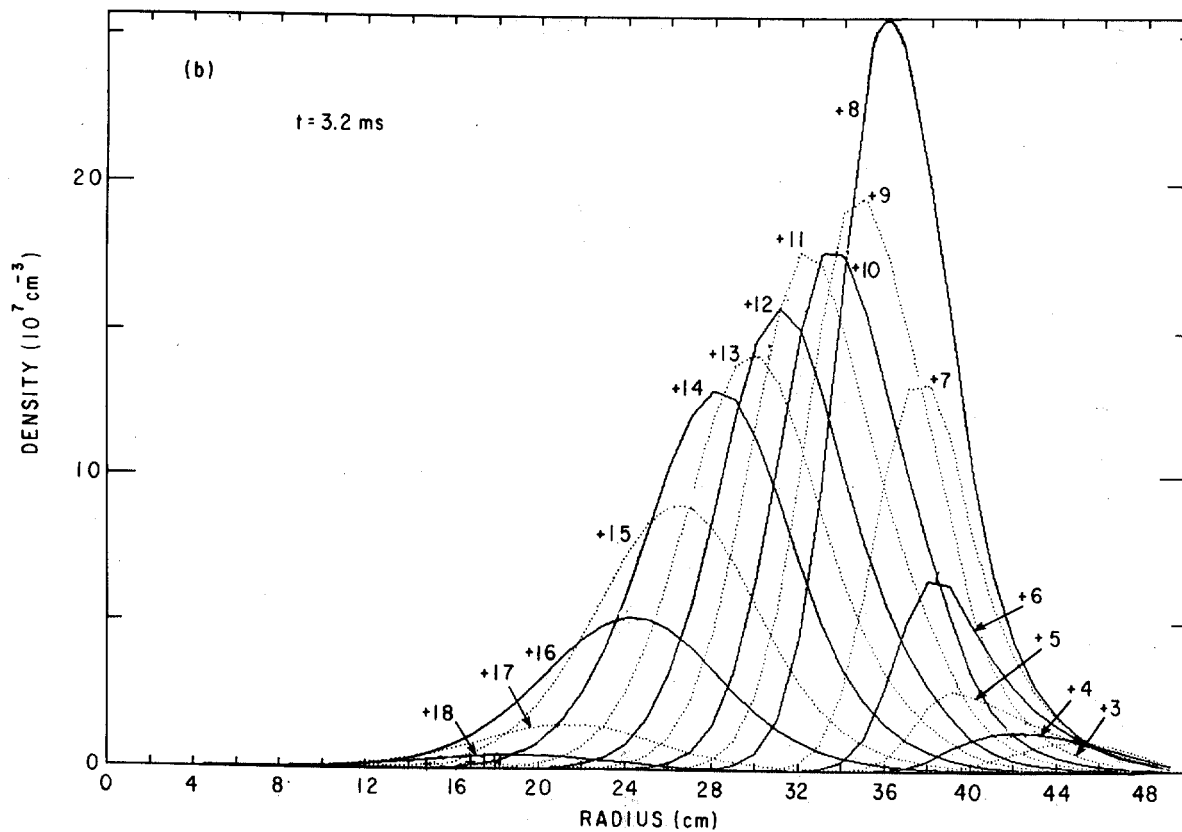
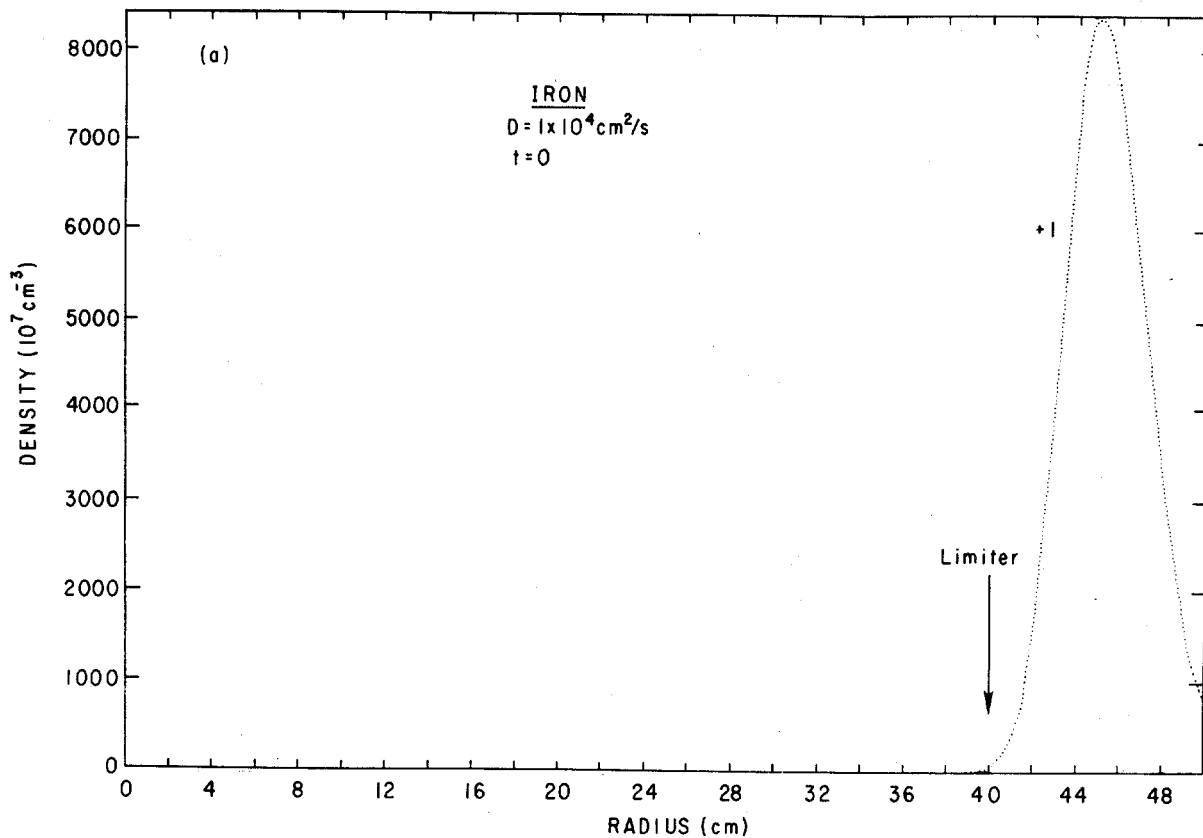


FIG. 6a,b

# 82P0148

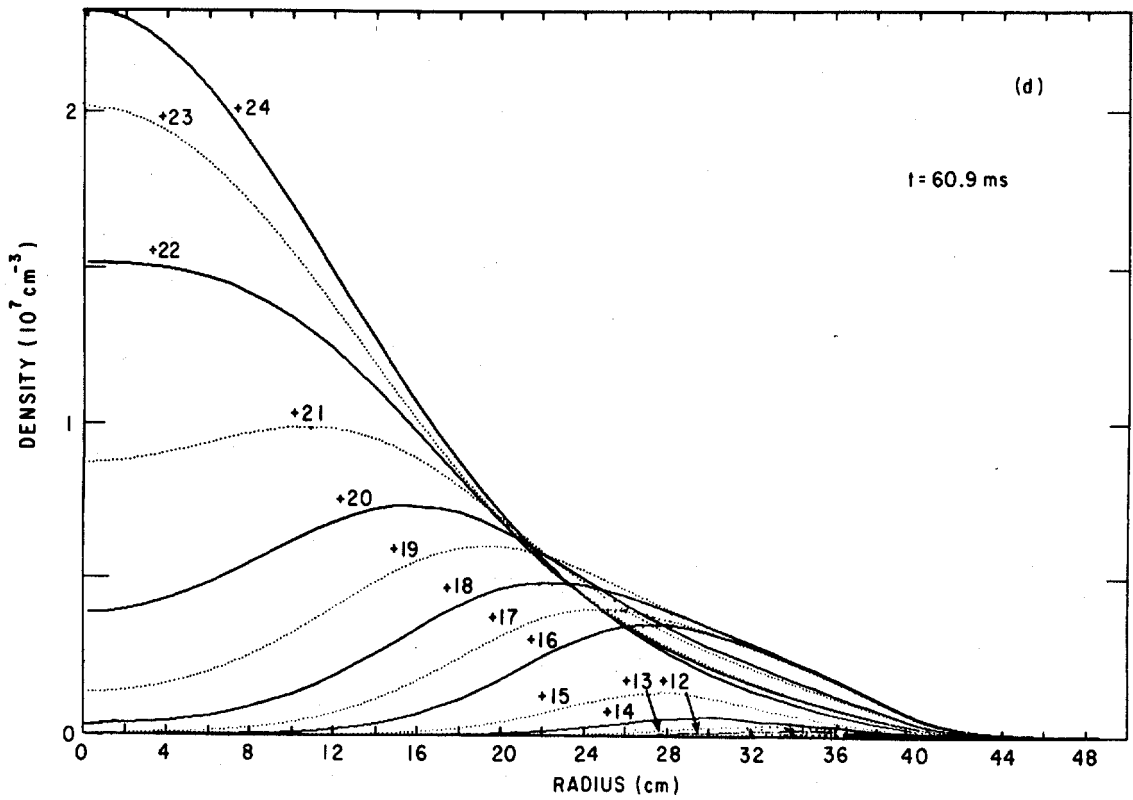
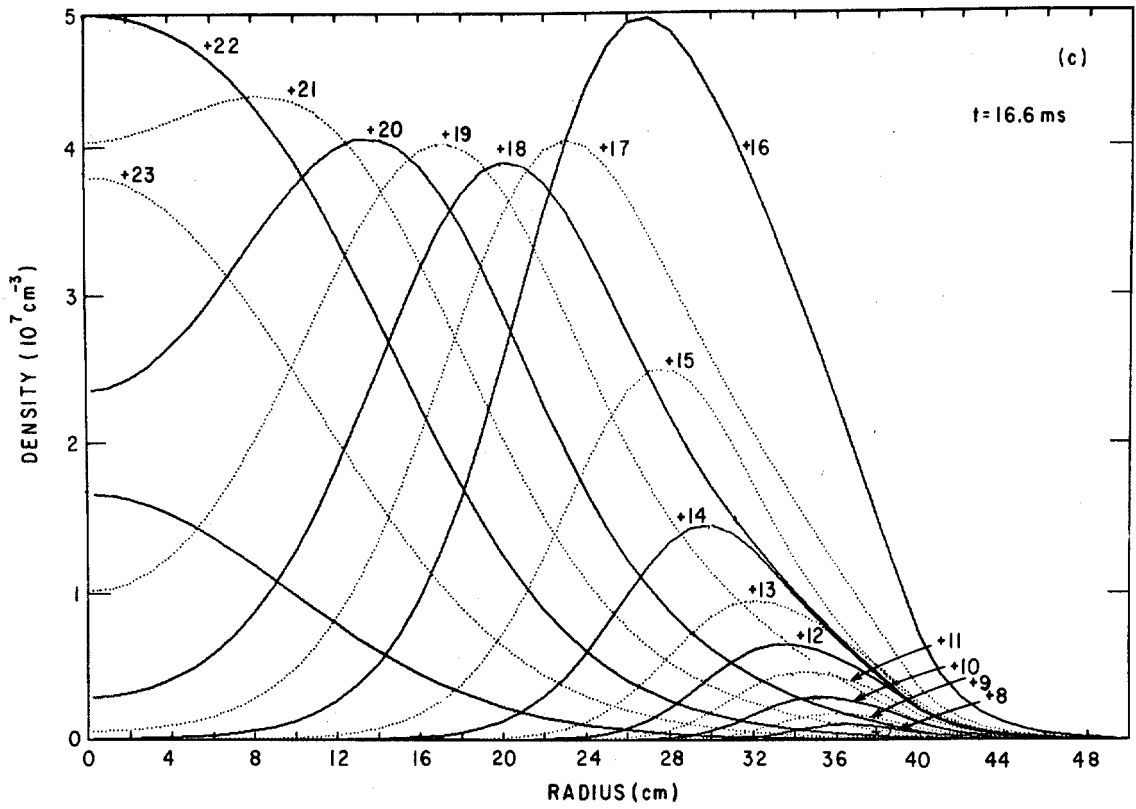


FIG. 6c,d

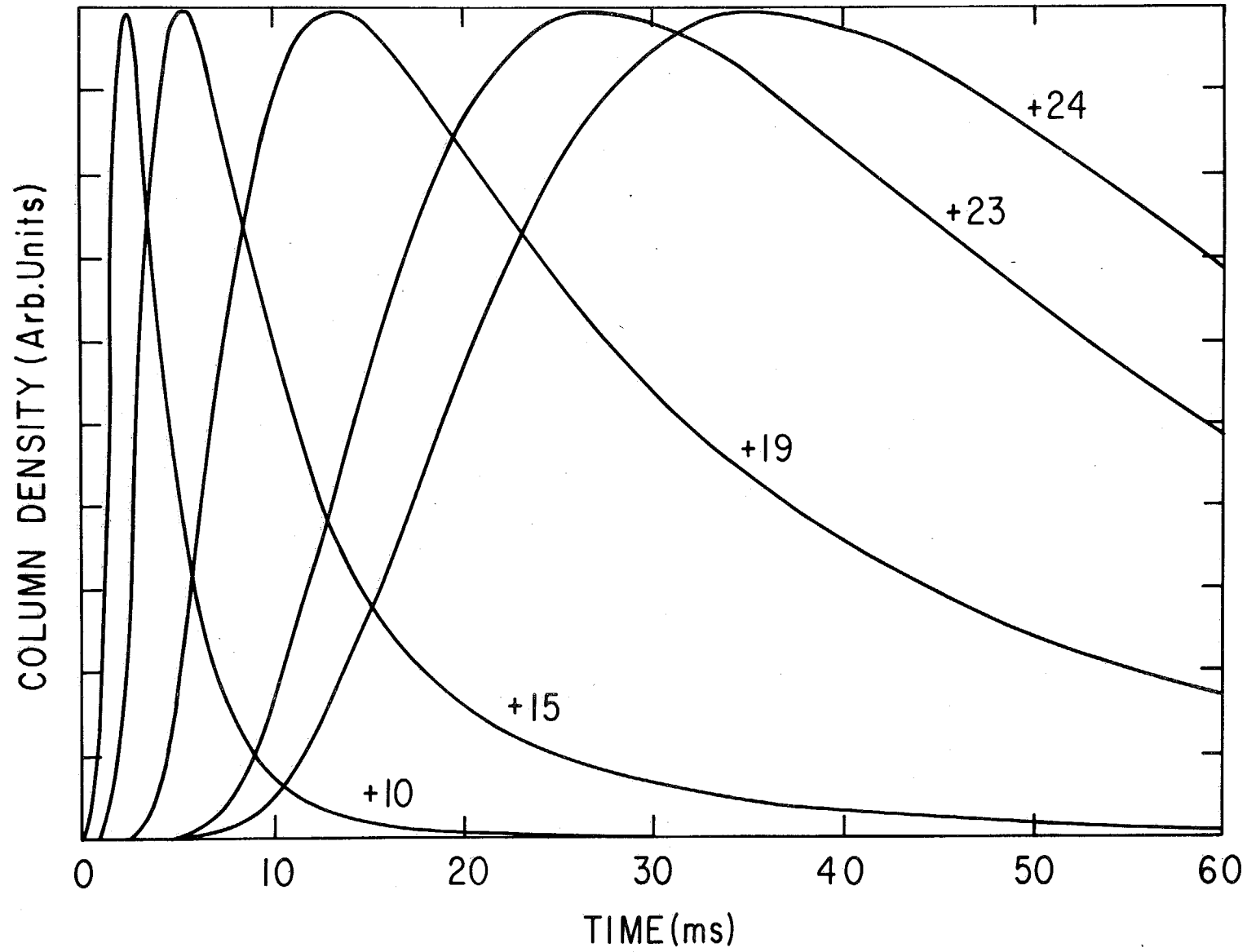


FIG. 7